Selective Laser Melting Fabrication of the Nickel Base Superalloy CMSX486: Optimisation of Process Parameters using Image Analysis and Statistical Methods

Carter, Luke; Essa, Khamis; Attallah, Moataz

DOI:
10.1108/RPJ-06-2013-0063

License:
Other (please specify with Rights Statement)

Document Version
Peer reviewed version

Citation for published version (Harvard):
Carter, L, Essa, K & Attallah, M 2015, 'Selective Laser Melting Fabrication of the Nickel Base Superalloy CMSX486: Optimisation of Process Parameters using Image Analysis and Statistical Methods', *Rapid Prototyping Journal*, vol. 21, no. 4. https://doi.org/10.1108/RPJ-06-2013-0063

Optimisation of Selective Laser Melting for a High Temperature Ni- Superalloy

Abstract

- **Purpose:** Selective Laser Melting (SLM) of high temperature nickel-base superalloys has had limited success due to the susceptibly of the material to solidification and reheat cracking. The aim of this study is to optimise the SLM process parameters for CMSX486 in order to produce a 'void-free' (fully consolidated) material, whilst reducing the cracking density to a minimum providing the best possible as-fabricated material for further post-processing.
- **Design/methodology/approach:** Samples of CMSX486 were fabricated by SLM. Statistical DOE (Design of Experiments) using the response surface method was used to generate an experimental design and investigate the influence of the key process parameters (laser power, scan speed, scan-spacing and island size). A stereological technique was used to quantify the internal defects within the material, providing two measured responses: cracking density and void percent.
- **Findings:** The analysis of variance (ANOVA) was used to determine the most significant process parameters and showed that laser power, scan speed and the interaction between the two are significant parameters when considering the cracking density. Laser power, scan speed, scan spacing and the interaction between power and speed, and, speed and spacing were the significant factors when considering void percent. The optimum setting of the process parameters that lead to minimum cracking density and void percent was obtained. It was shown that the nominal energy density can be used to identify a threshold for the elimination of large voids; however it does not correlate well to the formation of cracks within the material. To validate the statistical approach, samples were produced using the predicted optimum parameters in an attempt to validate the response surface model. The model showed good prediction of the void percent; however the cracking

results showed a greater deviation from the predicted value.

- **Originality/value (mandatory):** This is the first ever study on SLM of CMSX486. The paper shows that provided that the process parameters are optimised, SLM has the potential to provide a low cost route for the small-batch production of high-temperature aerospace components.

Keywords

Selective Laser Melting; Nickel Based Superalloys; Statistical Design of Experiments

1. Introduction

Additive Layer Manufacturing (ALM) covers a wide range of techniques including various forms of "3D-printing"; a succinct review of these techniques is presented by Levy *et al.* (Levy et al., 2003). SLM is an ALM technique in which successive layers of metal powder are selectively melted via a laser and bonded (via re-melting) to the previously built layers. This process is repeated until a netshaped three-dimensional geometry is built up by the combination of the two-dimensional slices.

The susceptibility of high γ′ volume fraction Ni-base superalloys to cracking due to SLM has been reported previously by Carter *et al.* (Carter et al., 2012) in CM247LC. Based on the microstructural observations it was found that under high specific-energy processing conditions, solidification cracking appears to be the dominant form of defect, transitioning to a dominance of grain-boundary cracking under lower specific-energy conditions (most likely by Ductility-Dip Cracking (DDC)) and finally the formation of large voids due to the incomplete consolidation of the material. Traditional welding literature provides much of the theoretical background on solidification cracking (DuPont et al., 2009) and the analysis by Dye *et al.* (Dye et al., 2001) who describes solidification cracking to occur within the solidifying material where the solidification stresses act on the remaining liquid in the inter-dendritic regions. DDC occurs due to the ductility trough occurring at intermediate temperature in many Ni-superalloys, the cracking behaviour within this region is characterised extensively by Collins *et al.* in a series of papers regarding Ni-base filler materials (Collins et al., 2003, Collins and Lippold, 2003, Collins et al., 2004). The research presented by Ramirez & Lippold (Ramirez and Lippold, 2004) discusses the mechanism for DDC describing it as failure due to stress concentrations around grain boundary carbides

occurring at a temperature high enough to allow for grain boundary sliding, but not dynamic recrystallisation. The microstructural observations of DDC made by Young *et al*. (Young et al., 2008) show void formation around the grain boundary carbides very similar in nature to the observations of cracks in SLM fabricated Ni-base superalloys made by Carter *et al*. (Carter et al., 2012).

CMSX486 (in a powder form) was selected for this study based on its high-temperature properties; the chemical composition of which is provided in Table 1:

Table 1: Chemical composition of CMSX486 (wt.%)

C	**Cr**	**Ni**	**Co**	**Mo**	**W**	**Ta**
0.07	5	Bal.	9.3	0.7	8.6	4.5
Ti	**Al**	**B**	**Zr**	**Hf**	**Re**	
0.7	5.7	0.015	0.005	1.2	3	

CMSX486 is a derivative of the single crystal alloy CMSX-4 with the addition of carbon to allow for some grain boundary strengthening, therefore, despite the 'SX' prefix, it is not a true single crystal alloy. The high levels of aluminium (γ' forming) and carbide grain-boundary strengthening in addition to the other minor elements largely providing solid-solution strengthening, making it very similarly in structure to CM247LC. As such the previous work carried out into SLM of CM247LC (Carter et al., 2012) can be used as a basis for this study in terms of the types of defects expected. Fundamental work relating to the structure and use of CMSX486 can be found in the research published by Harris and Wahl (Harris and Wahl, 2002, Harris and Wahl, 2004).

Previous studies have attempted to correlate the defect formation or material properties to a normalised 'energy density' parameter both in aluminium (Al-12Si) alloys (Olakanmi et al., 2011) and the nickel alloy Hastelloy X (Wu et al., 2011), equation (1). The dimensionless

'a1' parameter is the standard parameter for the control of scan spacing on the Concept Laser M2 as discussed in the experimental section.

$$\text{Nominal Energy Density}\,(J/mm^2) = \frac{Laser\ Power\,(W)}{Scan Speed\,(mm/s)\times Scan Spacing\,(a1)\times Focus Diameter\,(0.15mm)}$$

- Equation 1.

In these studies, the level of correlation between the measured responses to the nominal energy density varied with some responses showing a strong correlation to this value and other less so. For this study the energy density is as defined in Equation 1 based upon that used by Wu *et al.* (Wu et al., 2011) as the slice thickness was not a variable in the investigation; use of the J/mm^3 (as in (Olakanmi *et al.*, 2011)) would therefore be inappropriate. Alternatively, statistical approaches may provide a way to assess the influence of the process parameters, although physical interpretation of their outcomes can be difficult.

In this work a statistical DOE approach will be used to optimise the SLM parameters for a high γ′ Ni-base superalloy, CMSX486.

The response surface methodology is a statistical technique to generate an experimental design to find an approximate model between the input and output parameters and for the optimisation of process responses (Montgomery, 1997). It is a collection of statistical and mathematical methods that are useful for the modelling and analysing engineering problems. In this technique, the main objective is to optimise the response surface, which is influenced by various process parameters. The response surface, *Y*, can be expressed by a second order polynomial (regression) equation as shown in Equation 2.

$$Y = b_o + \sum b_i x_i + \sum b_i x_i^2 + \sum b_{ij} x_i x_j \qquad \textit{Equation 2}$$

The design procedure of response surface methodology is as follows:

- Selection of the process parameters.
- Selection of the upper and lower limit of the process parameters.
- Selection of the output response.
- Developing the experimental design matrix.
- Conducting the experiments as per the design matrix.
- Recording the output response.
- Developing a mathematical model to relate the process parameters with the output response.
- Optimising that model using genetic algorithm.

2. Experimental procedure

2.1 SLM fabrication

SLM samples were fabricated using the 'Concept Laser M2 Cusing Laser Powder-Bed' system located in the School of Metallurgy and Materials at the University of Birmingham. A schematic diagram of the M2 system is provided in Figure 1. It has a maximum build area of 250 mm × 250 mm and maximum build height of 300 mm. The M2 utilises a continuous wave fibre laser with a variable output (maximum 200 W) capable of scanning across the build platform at a maximum speed of 7000 mm/s with a fixed focus diameter of 150 μm. The scan spacing is represented using the 'a1' parameter by the Concept Laser software, a dimensionless number defined as:

a1 = Scan Spacing (μm) / Focus Diameter (150 μm)

All builds were carried out using a 20 μm slice thickness (Z-increment) under an Argon atmosphere, with oxygen levels maintained at < 0.1%.

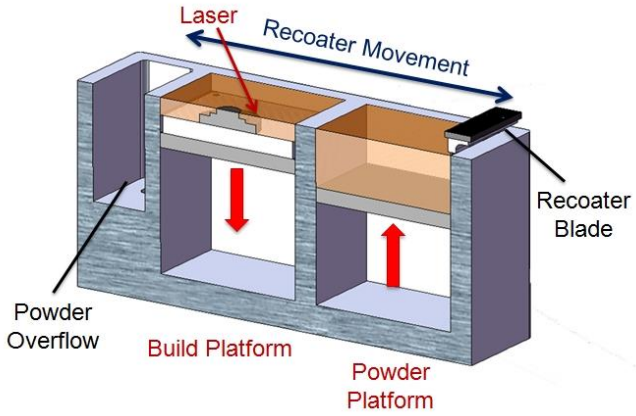

Figure 1: Schematic representation of the Concept Laser M2 Powder Bed Laser Cusing® facility. Each subsequent layer of powder is spread over the build area by the movement of the recoater blade and then selectively melted using the computer controlled laser.

As standard the Concept Laser M2 uses an island scan strategy (Figure 2). The filled area to be raster scanned is divided into small squares or 'islands', within each island, the laser spot is scanned in a single direction; perpendicular to the direction of adjacent islands. The islands are selectively melted in a random order in an attempt to balance the residual stresses (Hofmann, 2012). Following the selective melting of the islands, the laser is scanned around the outer-contour of the slice to refine the surface finish of the fabricated part and for each subsequent layer the island pattern is moved by 1 mm in both the X and Y directions to avoid defects due to overlapping island boundaries.

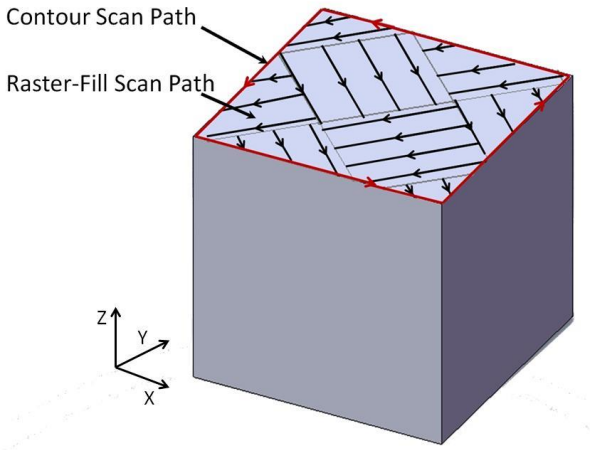

Figure 2: Schematic representation of the laser scanning regime for each layer.

For this investigation, cuboidal samples measuring 10 mm × 10 mm × 20 mm in the X, Y, Z dimensions were fabricated according to the design matrix as listed in Table 2.

2.2 Powder Characterisation

As a standard procedure, the particle size distribution of the powder was determined by a CoulterLS230 laser diffraction particle size analyser. The results are presented in Figure 3 and show that generally the powder lies in the desired range +15 – 53 µm with some fine particles although the fraction of these was not considered great enough to be of a detriment to the processability of the material.

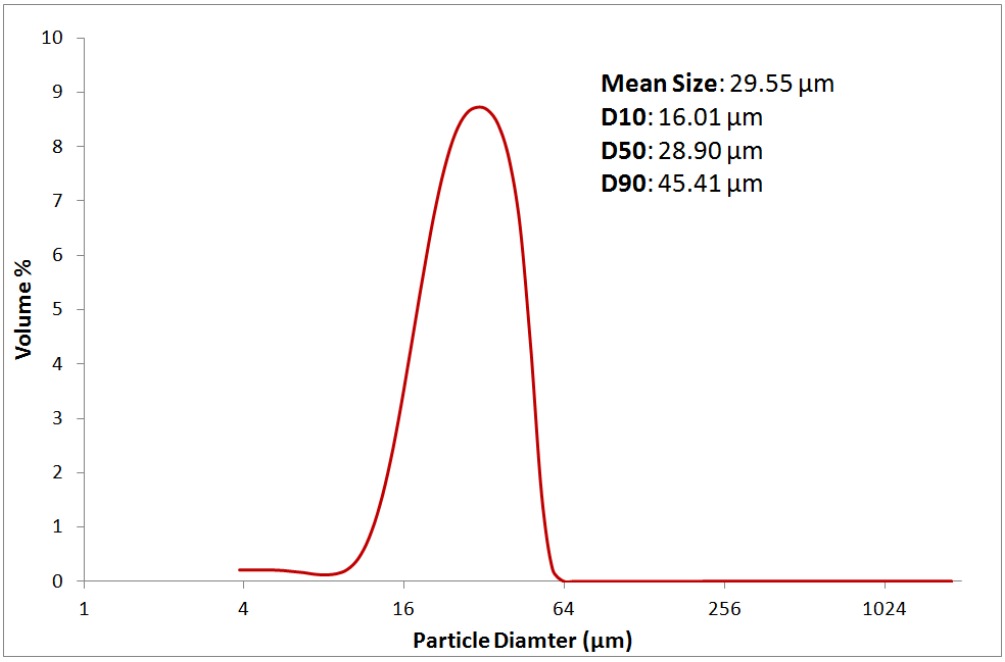

Figure 3: Particle size distribution for CMSX486 powder

A mounted and ground powder sample was examined as shown in Figure 4. In general the particles showed a reasonably spherical shape with some surface irregularities. Particles displayed a fine equiaxed grain structure and no noticeable elemental segregation under BSE SEM examination.

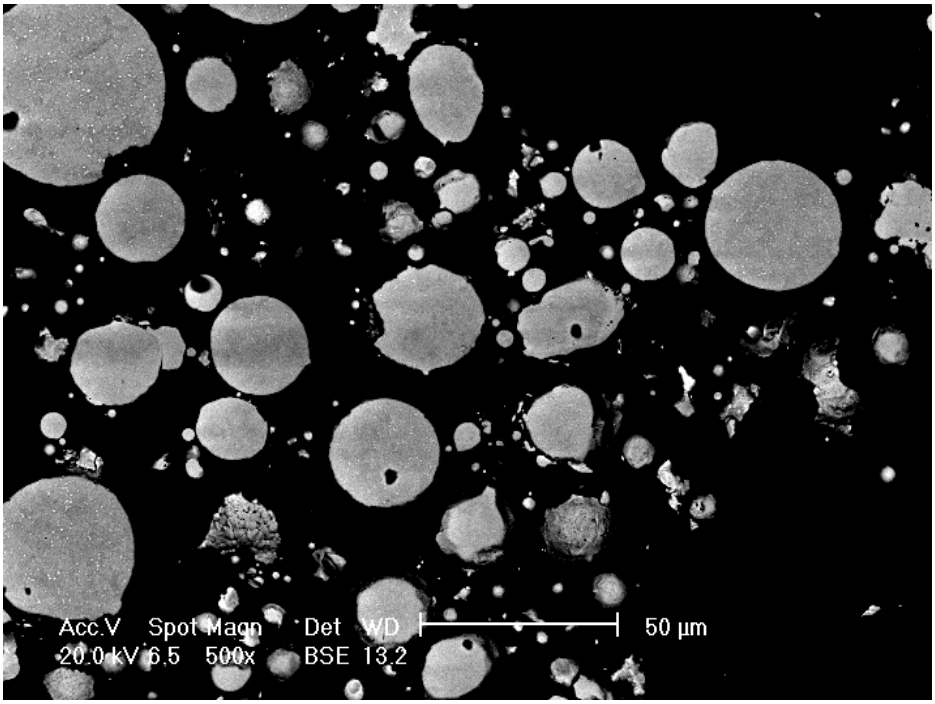

Figure 4: Backscattered SEM micrograph showing ground and polished CMSX486 powder sample

Many of the particles showed some gas porosity formed during the gas atomisation process and from a sample of 695 particles analysed by image analysis, an overall porosity of 0.87% was calculated for the powder.

2.3 The design of experiment

Laser power, scan speed, scan-spacing and island size have been identified in previous work (Carter et al., 2012) as being key parameters with regards to the structural integrity of the SLM processed material. For each parameter five levels were selected, evenly distributed in the design space. The overall range for the parameters was based on the limitation of the Concept Laser M2 and the previous work relating to CM247LC (Carter et al., 2012). The process parameters and their levels are provided in Table 1 covering a nominal energy density range of 0.64 – 4.00 J/mm^2. A five-level central composite rotatable response surface design was used to design the experimental matrix (Table 2). The output responses in this investigation were cracking density and the void percent.

Table 2: SLM process parameters and their levels

Parameter	Units	Levels				
		-2	-1	0	1	2
Laser Power	(W)	100	125	150	175	200
Scan Speed	mm/sec	500	1000	1500	2000	2500
Scan Spacing	-	0.2	0.35	0.5	0.65	0.8
Island Size	mm	2	3.5	5	6.5	8

2.4 Sample Preparation, Microscopy & Image Sampling

Samples were sectioned parallel to the build (Z) direction revealing the X-Z plane (Figure 5 (a)) and mounted. Samples were then ground and gradually polished to a final 0.05 μm alumina oxide finish.

Specimens were examined using a Phillips XL-30 SEM (LaB6 source) operated at 20 kV; Backscattered Electron (BSe) imaging provided a good contrast between the internal defects and the consolidated material, thus aiding the image analysis.

Sets of 21 images were collected for each sample in a regular pattern; 7 images were taken at 2 mm intervals along 3 lines running in the Z-direction. These lines were defined as beginning 2 mm from the sample base and 2 mm from the left side of the sample with line spacing being 3 mm (Figure 5). Each image covered an area ≈ 400 × 600 μm which covered a statistically sufficient population of defects.

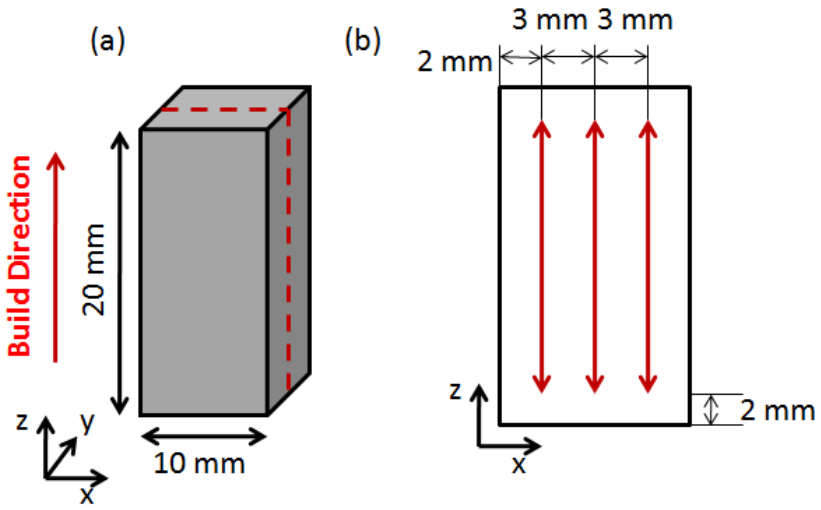

Figure 5: Diagram (not to scale) showing (a) sectioning plane of the sample (denoted by dashed line) and (b) image sampling method.

2.5 Image Analysis

ImageJ (Rasband) image analysis software was employed for the quantification of the defects within the samples. A threshold was applied to produce a binary image showing only the defects; both cracks and voids. Defects showing an area > 500 μm^2 were categorised as voids based on examination of the results and micrographs whereas all other defects were categorised as cracks. The area of the voids was summed for each set of 21 images (one sample) and presented as a % of the total micrograph area (void percent). The Feret Max. (F_{MAX}) of each of the cracks within each set of 21 images (one sample) was calculated as an approximation to crack length: cracks showing $F_{MAX} < 4$ μm (approximately the size of 1 pixel) were discarded as noise. Crack lengths for each set of 21 images were summed and divided by the entire micrograph area; this provided a cracking density in mm/mm^2. The stereological approach provides a better quantification for the defects based on their type, compared with overall density measurements which cannot distinguish between defect types.

The experimental design matrix and the recorded results are shown in Table 2.

Table 3: Experimental design matrix and results (randomised order).

Factor 1: Laser Power (W)	**Factor 2**: Scan Speed (mm/s)	**Factor 3**: Scan Spacing (a1)	**Factor 4**: Island Size (mm)	**Response 1**: Cracking Density (mm/mm^2)	**Response 2**: Void Percent (%)
150	1500	0.5	5	6.07	0.33
150	1500	0.5	2	8.16	0.50
100	1500	0.5	5	3.80	7.14
175	2000	0.65	3.5	5.32	6.48
150	1500	0.8	5	3.76	4.49
125	2000	0.35	6.5	3.92	3.18
125	1000	0.65	3.5	6.83	1.00
150	1500	0.5	8	6.05	0.07
125	1000	0.35	3.5	5.37	0.11
150	1500	0.5	5	5.87	0.04
175	2000	0.65	6.5	4.05	4.64
125	2000	0.65	3.5	2.41	22.43
125	2000	0.65	6.5	3.75	16.22
175	2000	0.35	3.5	6.57	0.32
200	1500	0.5	5	8.81	0.27
150	500	0.5	5	7.79	0.52
175	1000	0.35	6.5	5.96	0.73
150	2500	0.5	5	3.71	4.57
175	1000	0.65	3.5	8.66	0.21
175	1000	0.65	6.5	8.59	0.47
175	1000	0.35	3.5	5.86	0.21
175	2000	0.35	6.5	6.30	0.20
125	1000	0.65	6.5	4.03	0.26
125	1000	0.35	6.5	4.50	0.11
150	1500	0.5	5	6.88	0.10
125	2000	0.35	3.5	2.64	6.95
150	1500	0.2	5	6.81	0.27

2 Results Analysis & Discussion

3.1 Nominal Energy Density

The plot for both the void percent (%) and cracking density (mm/mm^2) against nominal energy density (J/mm^2) are shown in Figure 6. The plot shows a distinct threshold of nominal energy density (≈ 1.4 J/mm^2) for the elimination of large voids within the material (threshold of full consolidation). The cracking data does appear to show a very slight increase with nominal energy density and there is some indication of the grouping of points of similar

nominal energy densities, however there is also a large amount of scatter. It is likely that more complicated interactions are taking place that will be revealed by the statistical analysis.

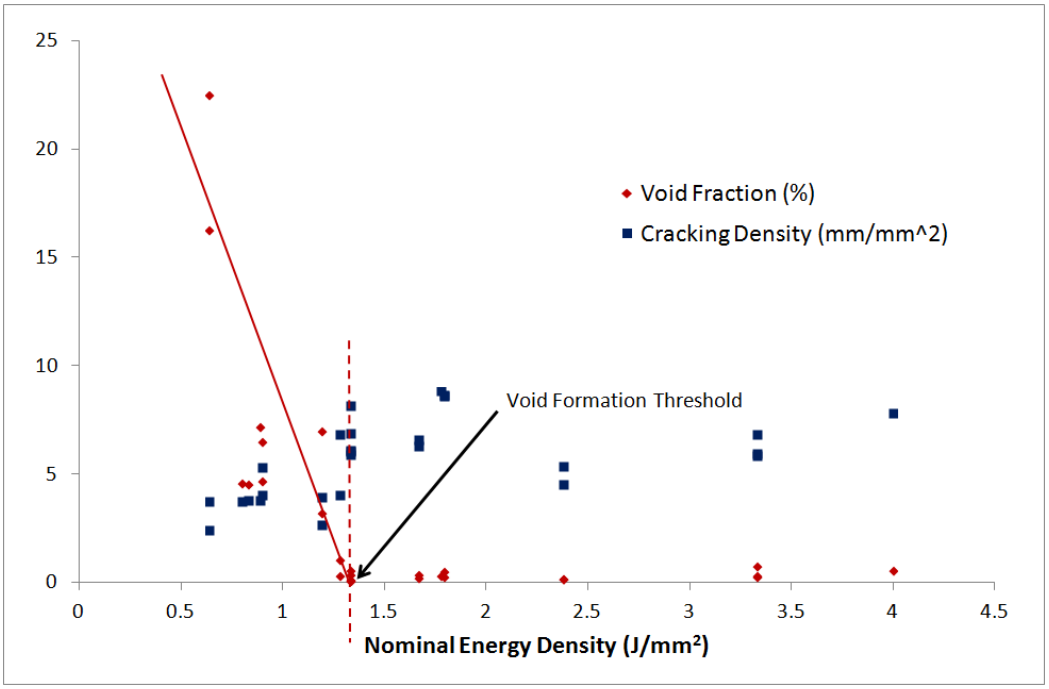

Figure 6: Scatter plot of raw cracking density and void percent data against nominal energy density; line indicates the data trend.

The similar study presented by Wu *et al.* (Wu et al., 2011) regarding HastelloyX shows a similar threshold for full consolidation (>99.5 % density) to occur at a nominal energy density of 1.5 J/mm^2 (a similar observation of a threshold for full consolidation is shown by Olakanmi *et al.*(Olakanmi et al., 2011) for Al alloys). The similarity of this threshold value for CMSX486 and HastelloyX suggests that it may be possible to link the process energy for consolidation to the energy required for melting however, further investigation involving other Ni-alloys and different alloy systems would be required to support this.

3.2 DOE Results

The response surface for cracking density and void percent is a function of laser power (*P*), scan speed (*S*), scan-spacing (*H*) and island size (*Z*) was constructed

The R-square value, a measure of model fit, showed that each of the models described the relationship between the process parameters and the output response (i.e., cracking density and void percent) reasonably. R-square was 80.12% for the cracking density model and 88.14% for the void percent model.

Table 3 shows the analysis of variance (ANOVA) P-values for each of the parameters and parameter interactions for the cracking density and void fraction. In statistical significance testing the p-value is the probability of obtaining a test statistic at least as extreme as the one that was actually observed, assuming that the null hypothesis is true. The null hypothesis (which assumes that all parameters have no significant influence) is rejected when the p-value is less than the predetermined significance level which is 0.05 (95% confidence level). This means that any factor has P-value less than 0.05 is considered to be a significant model parameter. The ANOVA indicates that cracking density is only effected by laser power (A), scan speed (B) and the interaction between scan speed and scan-spacing (BC). Void percent is effected by laser power (A), scan speed (B), scan-spacing (C), the interaction between the laser power and scan speed (AB) and the interaction between the scan speed and scan spacing (BC). Island size is unlikely to have any influence on either the cracking density or the void percent.

Table 4: Analysis of variance (ANOVA) P-values for each of the parameters and parameter interactions for the cracking density and void fraction.

	P-Value	
Model Parameters	**Cracking Density**	**Void Fraction**
A (Laser Power)	**0.0005**	**0.0023**
B (Scan Speed)	**0.0022**	**0.0003**
C (Scan Spacing)	0.5561	**0.0033**
D (Island Size)	0.2746	0.3522
AB	0.8126	**0.0047**
AC	0.7843	0.1001
AD	0.9270	0.3938
BC	**0.0490**	**0.0039**
BD	0.3489	0.2882
CD	0.5401	0.6410
$\mathbf{A^2}$	0.6357	0.0665
$\mathbf{B^2}$	0.3295	0.1543
$\mathbf{C^2}$	0.1702	0.1725
$\mathbf{D^2}$	0.7857	0.5906

Figure 7 (a) shows the response surface model prediction of cracking density with respect to laser power and scan speed. It shows that increasing scan speed and decreasing laser power, both reduce the cracking density. This can be related directly back to the specific energy input by the laser on the material. By reducing the laser power, increasing the scan speed or both, the specific energy input is reduced. As cracking is generally a result of residual stresses or solidification stresses (via various mechanisms), it is suggested that a reduction in energy input would result in lower residual stresses within the solidified material. This relationship between energy input (typically by adjusting weld speed) and residual stress within welding literature of nickel base superalloys is well reported with particulary significant paramteric studies being published by Rush *et al.* (Rush *et al.,* 2012) regarding Rene 80 and the studies by Egbewande *et al.* and Zhong *et al.* regarding Inconel 738 (Egbewande *et al.*, 2010, Zhong *et al.*, 2005).

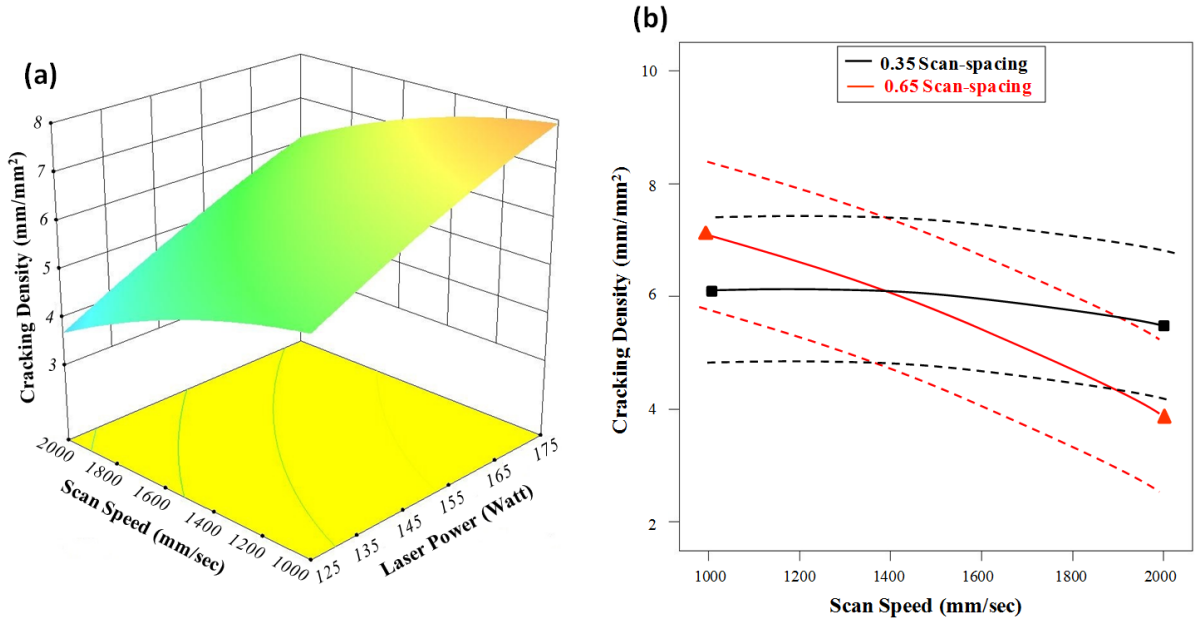

Figure 7: Plots showing: (a) the model effect of laser power and scan speed on the cracking density, at 0.5scan-spacing and 5.0mm island size; (b) the interaction effect of scan speed and scan-spacing on the cracking density, at 150 Watt laser power and 5.0 mm island size. The solid line represents model prediction while the dash lines represent the variation of the actual data around the model prediction

Figure 7 (b) shows the interaction between the scan speed and scan spacing on the cracking density. A low scan-spacing (0.35) results in almost eliminating the effect of scan speed on cracking density whereas a higher value of scan-spacing (0.65) reveals the previously stated relationship between scan speed and cracking density. It can be suggested that, as with the previous relationship discussed, the high energy input of a low scan-spacing is negating any positive effect a rapid scan speed may have on cracking density. This is difficult to support without further investigations into the residual stresses and thermal gradients generated during processing.

By considering the results presented in Figure 7 it has been shown that in order to reduce the cracking density; a low laser power, fast scan speed and large scan-spacing should be used for SLM processing.

Figure 8 (a) shows the response surface model prediction of void percent with respect to laser power and scan speed; it shows that decreasing laser power and increasing scan speed both result in an increased void percent. The influence of laser power on void percent is more significant at high scan speed and likewise the influence of scan speed is more significant at lower laser power; this interaction is discussed later (see Figure 9). Figure 8 (b) shows the response surface prediction of void percent with respect to scan-spacing and laser power; it shows that an increase in scan-spacing shows an increase in void percent.

A reduction in laser power and an increase in scan speed both have the effect of reducing the specific energy input into the material, as such these will result in shrinking the melt pool which will lead to the formation of voids due to incomplete consolidation and ultimately may lead to the breakdown of the SLM process. Likewise, an increase in scan-spacing will ultimately result in voids due to insufficient overlap between laser scan tracks and therefore incomplete consolidation.

By considering the results presented in Figure 8, it can be seen that in order to eliminate voids within the material, a high laser power, at low scan speed with a small scan-spacing should be used.

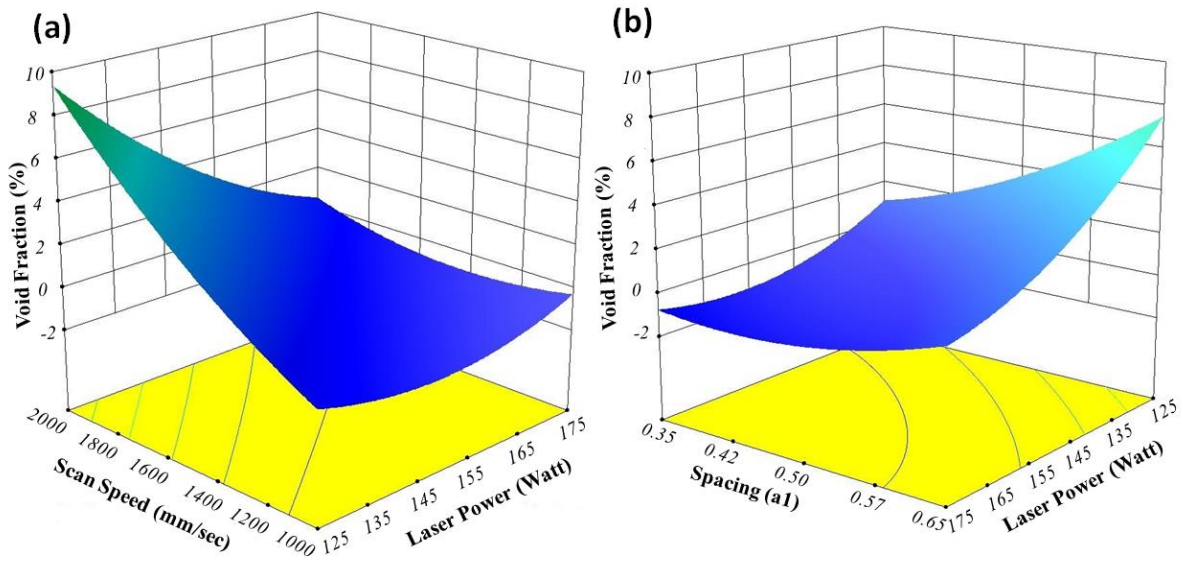

Figure 8: Plot showing the model effect of: (a) laser power and scan speed on the void percent, at 0.5scan-spacing and 5.0mm island size; (b) scan-spacing and laser power on the void percent, at 1500mm/sec scan speed and 5.0mm island size

Figure 9 (a) shows the interaction effect between laser power and scan speed on the void percent. A low scan speed (1000 mm/sec) appears to eliminate the effect of laser power on the void percent; whereas a high scan speed (2000 mm/sec) significantly increases the effect of laser power on void percent.

Figure 9 (b) shows the interaction effect between the scan speed and scan spacing on the void percent. A low scan-spacing (0.35) appears to eliminate the effect of scan speed on the void percent; whereas a high scan-spacing (0.65) significantly increases the effect of scan speed on void percent.

As void percent cannot be reduced below zero it can be suggested that a certain threshold of input energy is required in order to produce full consolidation. In this way the influence of either the laser power or the scan speed (or theoretically the scan-spacing) can be mitigated by compensating by using one of the other parameters to increase the energy input (e.g.

scanning the laser slowly enough will produce full consolidation for all the laser powers investigated within the design space). This suggestion of an energy threshold for full consolidation is supported by the raw data previously shown in Figure 6.

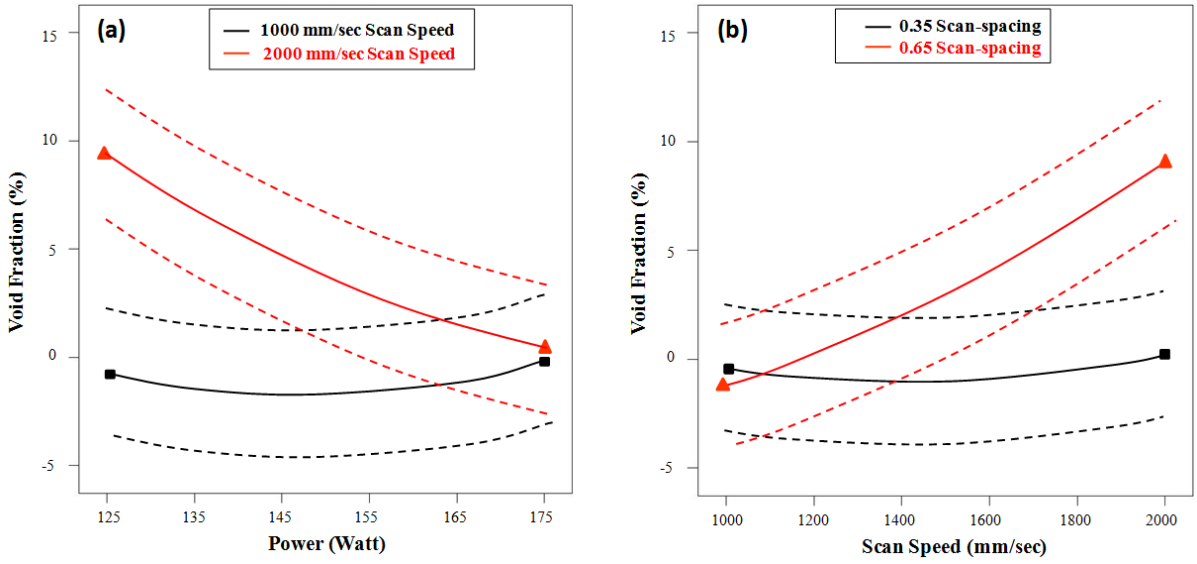

Figure 9: The interaction effect of (a) laser power and scan speed on the void percent, at 0.5scan-spacing and 5.0mm island size and (b) scan speed and scan spacing on the void percent, at 150Watt laser power and 5.0mm island size. The solid line represents model prediction while the dash lines represent the variation of the actual data around the model prediction

Simultaneous consideration of the influence of the parameters on the cracking density and the void percent results in an immediate problem. In order to reduce the cracking density; a low laser power, high scan speed and large scan-spacing should be used. This is the exact opposite to the requirements needed to produce full consolidation and a zero void percent material. Purely based on this, it can be seen that, for CMSX486 processed by the Concept Laser M2, no possible combination of the four investigated parameters will result in a fully dense material showing no cracks.

3.3 Process Optimisation

During the optimisation, the objective function was set to minimise the cracking density whilst maintaining a zero (or effectively zero) void percent; the genetic algorithm was used to predict process parameters based on the objective function. The equations modelling the response of cracking density and void percent with respect to the four key process parameters were solved simultaneously.

3.4 Validation

Process parameters of 128 W laser power, 1007 mm/sec scan speed, 0.63 scan-spacing and 6.4 mm island size were predicted to be optimal based on the model. Using these parameters in the SLM of CMSX486, a predicted cracking density of 5.4 mm/mm^2 (Figure 10 (a)) and a void percent of 0.0006% (Figure 10 (b)) were predicted.

A validation sample was produced using these process parameters and analysed as before, the results of which are shown in Table 4. The predicted void percent shows a good agreement with the results from the validation sample. The cracking density shows less agreement and suggests that the scatter within the cracking density is much greater than that seen within the void percent results. This is due to the fact that, R-square (measure of the statistical significance of the fit) for the cracking density model is less than that for the void percent model. It is possible that future studies may be able to reduce the influence of scatter caused by sampling a greater number of micrographs, or examining multiple samples processed under the same parameters in order to gain a larger data set in which to base the response surface fit. Additionally the use of MicroCT to obtain a three-dimensional assessment of the cracking density may provide a more accurate value than the two-dimensional sectioning.

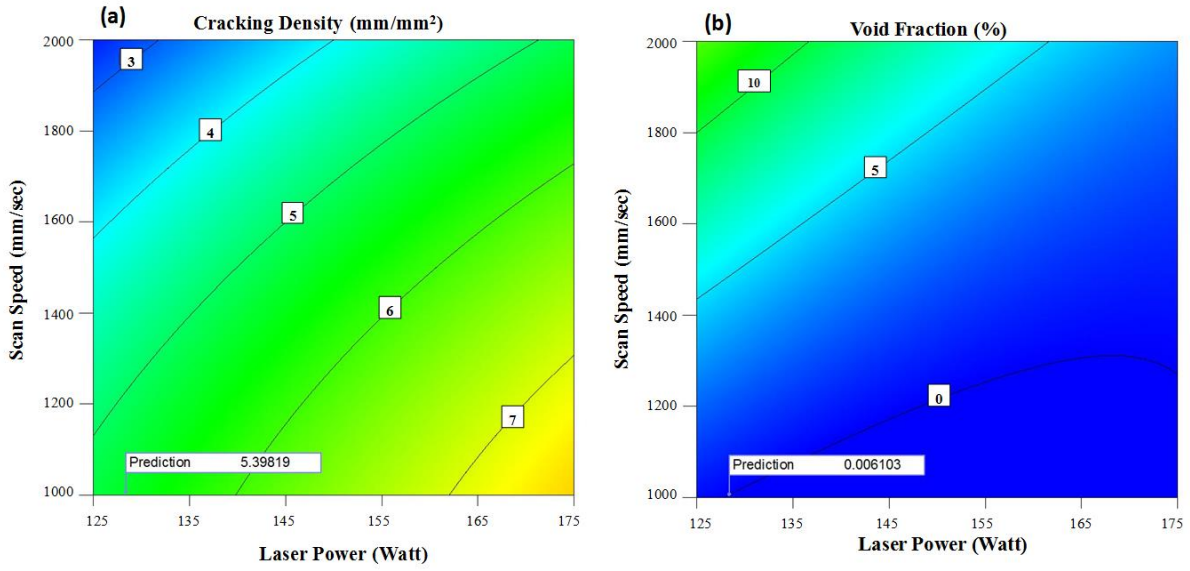

Figure 10: Predicted optimum laser power and scan speed for (a) minimum cracking density and (b) zero void percent within the SLM system parameter's range.

Table 5: The predicted and measured responses for cracking density and void percent using for the predicted optimum process parameters.

Response	Predicted	Measured
Cracking density (mm/mm^2)	5.40	2.24
Void percent (%)	0.006	0.00

3.5 Microstructure Observations

Although the microstructural development due to SLM is outside the scope of this investigation, typical micrographs are included to illustrate the different defects observed during image analysis and the improvement made due to the optimisation process. Figure 11 shows a typical micrograph used for image analysis from a sample showing low-porosity, but relatively high levels of cracking (150 W, 1500 mm/s, 0.5(a1), 2 mm islands). Note the combination of jagged solidification style cracks and the smoother more directional grain-boundary style cracks.

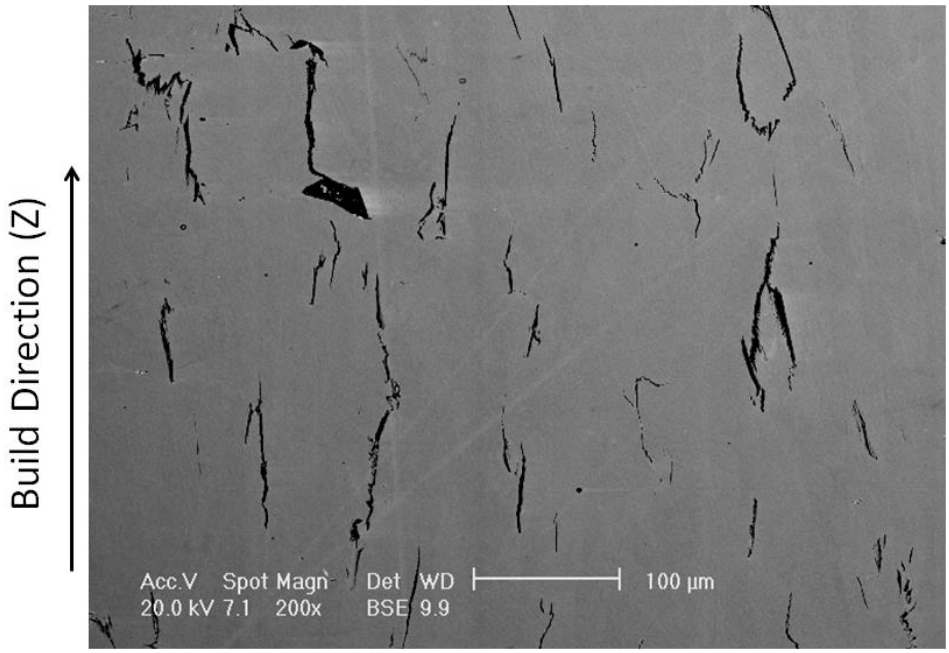

Figure 11: BSE SEM micrograph showing cracked sample with low void percent (150 W, 1500 mm/s, 0.5(a1), 2 mm islands).

Figure 12 shows a typical micrograph used for image analysis from a sample showing relatively high void percent (100 W, 1500 mm/s, 0.5(a1), 5 mm islands). These voids are formed due to the low nominal energy density (1.33 J/mm^2) conditions used during processing resulting in incomplete consolidation of the material.

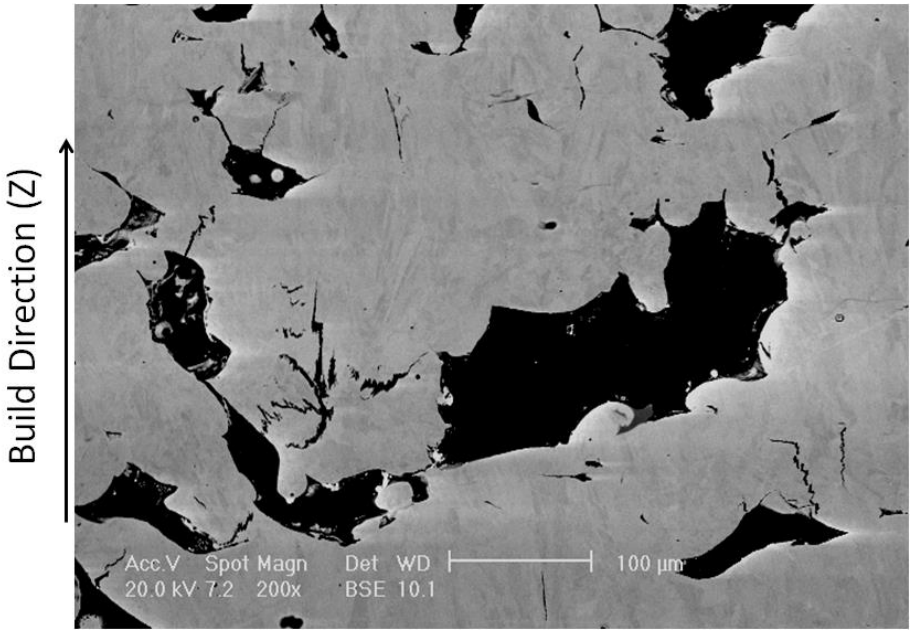

Figure 12: BSE SEM micrograph showing sample with high void percent (100 W, 1500 mm/s, 0.5(a1), 5 mm islands).

Figure 13 shows a typical micrograph used for image analysis from the validation sample built using the model best parameters. It does not show significant voids and has a relatively low cracking density when compared to the sample in Figure 11. Grain boundary cracks (arrowed) and some small isolated pores (circled) have been indicated.

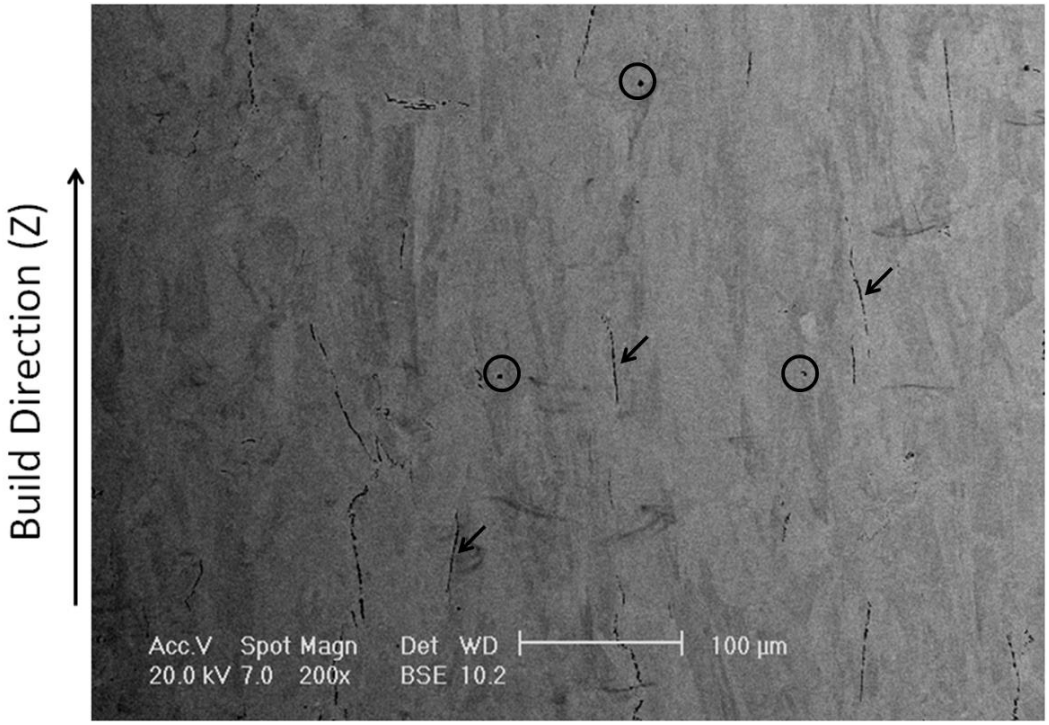

Figure 13: BSE SEM micrograph showing sample built using model best parameters; Grain boundary cracks (arrowed) and some small isolated pores (circled) have been indicated.

4 Conclusions

In this study, a statistical method was used to rapidly assess the process parameters for SLM using stereological analysis of the defects present. A model has been produced for CMSX486 to show the trends in cracking density and void percent present within SLM fabricated

samples. This model has shown that the ideal parameters to reduce cracking, and those to reduce void percent are not compatible and therefore a compromise between the two is inevitable. The void formation can be related strongly to the input nominal energy density by the laser and both the model and raw data have shown there to be a threshold value at which voids are no longer observed. The cracking behaviour is more complicated and does not show such a strong relationship to the input nominal energy density; it is likely an inherent response of the material to the laser and as such further in depth studies would be required to govern the driving factors behind this. For the process optimisation a zero void percent condition (judged to be the more detrimental form of defect) should be maintained whilst reducing the cracking to a minimum within the design space. Predicted optimum conditions were generated and a validation sample showed good agreement to the predicted for void percent, however the agreement between measured cracking density and the predicted was poorer.

5 Acknowledgements

The authors would like to acknowledge the support of our collaborators from MicroTurbo/Safran Group. LNC would like to acknowledge the financial support provided by the Engineering and Physical Sciences Research Council (EPSRC) for his PhD Scholarship.

6 References

CARTER, L. N., ATTALLAH, M. A. & REED, R. C. (2012) Laser Powder Bed Fabrication of Nickel-Base Superalloys: Influence of Parameters; Characterisation, Quantification and Mitigation of Cracking. *Superalloys 2012***,** 577-608.

COLLINS, M. G. & LIPPOLD, J. C. (2003) An investigation of ductility dip cracking in nickel-based filler materials - Part I. *Welding Journal (Miami, Fla)*, 82**,** 288/S-295/S.

COLLINS, M. G., RAMIREZ, A. J. & LIPPOLD, J. C. (2003) An Investigation of Ductility Dip Cracking in Nickel-Based Weld Metals - Part II. *Welding Journal (Miami, Fla)*, 82**,** 348S-354S.

COLLINS, M. G., RAMIREZ, A. J. & LIPPOLD, J. C. (2004) An investigation of ductility-dip cracking in nickel-based weld metals - Part III. *Welding Journal (Miami, Fla)*, 83**,** 39/S-49/S.

DUPONT , J. N., LIPPOLD, J. C. & KISER, S. D. (2009) *Welding Metallurgy and Weldability of Nickel-Base Alloys*, Wiley.

DYE, D., HUNZIKER, O. & REED, R. C. (2001) Numerical analysis of the weldability of superalloys. *Acta Materialia*, 49**,** 683-697.

EGBEWANDE, A. T., BUCKSON, R. A. & OJO, O. A. (2010) Analysis of laser weldability of Inconel 738 superalloy, *Materials Characterization*, 61, 569-574.

HARRIS, K. & WAHL, J. B. (2002) CMSX-486, a new grain boundary strengthened single crystal superalloy, Amsterdam, Netherlands, *American Society of Mechanical Engineers*, 3B, 1163-1180.

HARRIS, K. & Wahl, J. B. (2004). *Improved single crystal superalloys, CMSX-4 (SLS)[La+Y] and CMSX-486*, Champion, PA, United states, *Minerals, Metals and Materials Society*. 45-52.

HOFMANN (2012) Hofmann Innovation Group Website - Concept Laser (http://www.hofmann-innovation.com/en/technologies/direct-cusing-manufacturing.html).

LEVY, G. N., SCHINDEL, R. & KRUTH, J. P. (2003) Rapid manufacturing and rapid tooling with layer manufacturing (LM) technologies, state of the art and future perspectives. *CIRP Annals - Manufacturing Technology*, 52**,** 589-609.

MONTGOMERY, D. C. (1997) *Design and Analysis of Experiments (4th Edition)*, New York, John Wiley & Sons.

OLAKANMI, E. O., COCHRANE, R. F. & DALGARNO, K. W. (2011) Densification mechanism and microstructural evolution in selective laser sintering of Al-12Si powders. *Journal of Materials Processing Technology*, 211**,** 113-121.

RAMIREZ, A. J. & LIPPOLD, J. C. (2004) High temperature behavior of Ni-base weld metal Part II - Insight into the mechanism for ductility dip cracking. *Materials Science and Engineering A*, 380**,** 245-258.

RASBAND, W. ImageJ 1.34u. National institutes of health.

RUSH, M. T., COLEGROVE, P. A., ZHANG, Z. & BROAD, D. (2012) Liquation and post-weld heat treatment cracking in Rene 80 laser repair welds. *Journal of Materials Processing Technology*, 212, 188-197.

WU, X., WANG, F. & CLARK, D. (2011) On direct laser deposited Hastelloy X: dimension, surface finish, microstructure and mechanical properties. *Materials Science and Technology*, 27**,** 344 - 356.

YOUNG, G. A., CAPOBIANCO, T. E., PENIK, M. A., MORRIS, B. W. & MCGEE, J. J. (2008) The mechanism of ductility dip cracking in nickel-chromium alloys. *Welding Journal (Miami, Fla)*, 87**,** 31-s-43-s.

ZHONG, M., HONGQING, S., WENJIN, L., XIAOFENG, Z. & JINJIANG, H. (2005) Boundary liquation and interface cracking characterization in laser deposition of Inconel 738 on directionally solidified Ni-based superalloy. *Scripta Materialia*, 53, 159-164.

List of Figure Captions

Figure 1: Schematic representation of the Concept Laser M2 Powder Bed Laser Cusing® facility. Each subsequent layer of powder is spread over the build area by the movement of the recoater blade and then selectively melted using the computer controlled laser.

Figure 2: Schematic representation of the laser scanning regime for each layer.

Figure 3: Particle size distribution for CMSX486 powder

Figure 4: Backscattered SEM micrograph showing ground and polished CMSX486 powder sample

Figure 5: Diagram (not to scale) showing (a) sectioning plane of the sample (denoted by dashed line) and (b) image sampling method.

Figure 6: Scatter plot of raw cracking density and void percent data against nominal energy density; line indicates the data trend.

Figure 7: Plots showing: (a) the model effect of laser power and scan speed on the cracking density, at 0.5scan-spacing and 5.0mm island size; (b) the interaction effect of scan speed and scan-spacing on the cracking density, at 150 Watt laser power and 5.0 mm island size. The solid line represents model prediction while the dash lines represent the variation of the actual data around the model prediction

Figure 8: Plot showing the model effect of: (a) laser power and scan speed on the void percent, at 0.5scan-spacing and 5.0mm island size; (b) scan-spacing and laser power on the void percent, at 1500mm/sec scan speed and 5.0mm island size

Figure 9: The interaction effect of (a) laser power and scan speed on the void percent, at 0.5scan-spacing and 5.0mm island size and (b) scan speed and scan spacing on the void

percent, at 150Watt laser power and 5.0mm island size. The solid line represents model prediction while the dash lines represent the variation of the actual data around the model prediction

Figure 10: Predicted optimum laser power and scan speed for (a) minimum cracking density and (b) zero void percent within the SLM system parameter's range.

Figure 11: BSE SEM micrograph showing cracked sample with low void percent (150 W, 1500 mm/s, 0.5(a1), 2 mm islands).

Figure 12: BSE SEM micrograph showing sample with high void percent (100 W, 1500 mm/s, 0.5(a1), 5 mm islands).

Figure 13: BSE SEM micrograph showing sample built using model best parameters; Grain boundary cracks (arrowed) and some small isolated pores (circled) have been indicated.

List of Tables